The Journal of Pathology: Clinical Research
J Path: Clin Res October 2016; **2:** 210–222
Published online 18 April 2016 in Wiley Online Library (wileyonlinelibrary.com). DOI: 10.1002/cjp2.49

Original Article

Quantitative imaging for development of companion diagnostics to drugs targeting HGF/MET

Fangjin Huang,[1] Zhaoxuan Ma,[1] Sara Pollan,[1] Xiaopu Yuan,[1] Steven Swartwood,[1] Arkadiusz Gertych,[2] Maria Rodriguez,[1] Jayati Mallick,[3] Sanica Bhele,[3] Maha Guindi,[3] Deepti Dhall,[3] Ann E Walts,[3] Shikha Bose,[3] Mariza de Peralta Venturina,[3] Alberto M Marchevsky,[3] Daniel J Luthringer,[3] Stephan M Feller,[4] Benjamin Berman,[1] Michael R Freeman,[1,2,5] W Gregory Alvord,[6] George Vande Woude,[7] Mahul B Amin[3] and Beatrice S Knudsen[1,3]*

[1] *Department of Biomedical Sciences, Cedars-Sinai Medical Center, Los Angeles, California 90048, USA*
[2] *Departments of Surgery, Cedars-Sinai Medical Center, Los Angeles, California 90048, USA*
[3] *Department of Pathology and Laboratory Medicine, Cedars-Sinai Medical Center, Los Angeles, California 90048, USA*
[4] *Institute of Molecular Medicine, Martin-Luther-University, 06120, Halle, Germany*
[5] *Cancer Biology Program, Departments of Medicine, Samuel Oschin Comprehensive Cancer Institute, Cedars-Sinai Medical Center, Los Angeles, California 90048, USA*
[6] *Data Management Services, Inc., National Cancer Institute at Frederick, Frederick, Maryland 21702, USA*
[7] *Laboratory of Molecular Oncology, Center for Cancer and Cell Biology, Van Andel Research Institute, Grand Rapids, Michigan 49503, USA*

**Correspondence to: Beatrice S Knudsen, Department of Pathology and Laboratory Medicine, Cedars-Sinai Medical Center, Los Angeles, California 90048, USA. e-mail: beatrice.knudsen@cshs.org*

Abstract

The limited clinical success of anti-HGF/MET drugs can be attributed to the lack of predictive biomarkers that adequately select patients for treatment. We demonstrate here that quantitative digital imaging of formalin fixed paraffin embedded tissues stained by immunohistochemistry can be used to measure signals from weakly staining antibodies and provides new opportunities to develop assays for detection of MET receptor activity. To establish a biomarker panel of MET activation, we employed seven antibodies measuring protein expression in the HGF/MET pathway in 20 cases and up to 80 cores from 18 human cancer types. The antibodies bind to epitopes in the extra (EC)- and intracellular (IC) domains of MET ($MET4^{EC}$, $SP44\_MET^{IC}$, $D1C2\_MET^{IC}$), to MET-pY1234/pY1235, a marker of MET kinase activation, as well as to HGF, pSFK or pMAPK. Expression of HGF was determined in tumour cells (T_HGF) as well as in stroma surrounding cancer (St_HGF). Remarkably, $MET4^{EC}$ correlated more strongly with pMET ($r = 0.47$) than $SP44\_MET^{IC}$ ($r = 0.21$) or $D1C2\_MET^{IC}$ ($r = 0.08$) across 18 cancer types. In addition, correlation coefficients of pMET and T_HGF ($r = 0.38$) and pMET and pSFK ($r = 0.56$) were high. Prediction models of MET activation reveal cancer-type specific differences in performance of $MET4^{EC}$, $SP44\_MET^{IC}$ and anti-HGF antibodies. Thus, we conclude that assays to predict the response to HGF/MET inhibitors require a cancer-type specific antibody selection and should be developed in those cancer types in which they are employed clinically.

Keywords: HGF/MET; multi-cancer tissue microarray; quantitative imaging

Received 6 January 2016; Accepted 7 April 2016

The authors declare no conflict of interest.

Introduction

Immunohistochemistry (IHC) is widely used clinically to aid with challenging diagnostic decisions that require formalin-fixed and paraffin embedded (FFPE) tissues. In the era of precision medicine, the ease associated with detecting proteins and phosphoproteins in single cancer cells via IHC is ideal for development of companion diagnostics needed to stratify patients for treatment with targeted therapies. However, technical problems diminishing the accuracy of quantifying the expression of drug targets by IHC hinder this biomarker development. The recent emergence of whole slide imaging and digital image analysis generates quantitative numerical data associated with protein expression in FFPE tissues [1,2]. In theory, this approach could provide new opportunities for measuring the expression of drug targets in

cancer tissues obtained from patients during routine medical care. However, the use of digital image analysis for biomarker development and companion diagnostics is still in its infancy [1] because it requires multidisciplinary interactions between pathologists, experts in image processing and software developers.

The MET receptor tyrosine kinase is a documented oncoprotein in human cancer (visual database available here: http://www.vai.org/met/). Our and other groups linked MET to epithelial-to-mesenchymal transition, invasion and metastasis in human cancer cells and in mouse models [3]. Germline activating mutations of MET cause hereditary papillary renal carcinoma and MET expression is associated with adverse outcome in practically all solid tumours [4,5]. In addition, the human *MET* gene lies in an unstable genomic region on chromosome 7 that is prone to amplification [6,7]. Hence, clonal expansion of cancer cells with multiple copies of the *MET* gene or with autocrine production of the MET ligand, Hepatocyte Growth Factor/Scatter Factor (HGF), can cause resistance to drugs that inhibit other receptor tyrosine kinases [8]. The key role of MET in oncogenesis and drug resistance provides a strong rationale for extensive drug development [9]. While most clinical trials with MET kinase inhibitors have not demonstrated an overall survival advantage, a subset of patients clearly experienced cancer control [10].

The lack of appropriate companion diagnostics compromises the success of clinical trials with MET inhibitors [11] and the limited success may stem from inadequate selection of patients. Measuring the active MET kinase, ie, the drug target, relies on detection of protein phosphorylation, which constitutes an inherently unstable posttranslational modification. In addition, biomarker development is complicated by the sequestration of MET in signalling endosomes and shedding from the cell surface [12,13]. Companion diagnostic assays for MET inhibitors employed *MET* FISH and MET IHC [14]. However, association of these measurements with activation of the MET kinase varies among cancer types [15]. Because of extensive post-translational regulation of MET protein expression, MET mRNA expression has not been explored as a biomarker of MET activation. Furthermore IHC to measure MET protein expression has not been stringently validated in FFPE tissues [16]. Collectively, the different mechanisms of MET kinase activities, ie, genomic mutations, binding of HGF and overexpression and/or crosstalk with other cell surface receptors [3,17], have so far not resulted in the development of a uniform assay of MET receptor activation.

To analyze the activation of the MET pathway, we generated a tissue microarray (TMA) of 18 different cancer types. We employed seven antibodies that react with proteins in the MET pathway. SP44_MET^{IC} and D1C2_MET^{IC} bind epitopes within the cytoplasmic C-terminus of MET and MET4^{EC} recognizes a motif in the MET receptor alpha-chain, which is extracellular [18]. We also utilized an antibody reactive with HGF. To determine the activation of cytoplasmic MET signalling pathways, we selected antibodies that bind phospho-MAPK and phospho-SRC-family kinases (SFK). Using quantitative digital imaging of slides stained by IHC, we generated a dataset consisting of 9139 individual measurements. The analysis of the data revealed that antibodies most predictive of MET activation differ amongst cancer types. This approach highlights the importance of cancer-type specific development of companion diagnostic assays for drugs against the active MET receptor kinase.

Materials and methods

Selection of cases and TMA construction

For TMA construction, 20 cases from 18 cancer types, which were randomly retrieved from the pathology archive, were displayed and confirmed by a subspecialty pathologist (Dataset S1 and Table S1). The MET genomic status was presumed to be identical to germline [19]. The core diameter was 0.6 mm except for sarcoma, melanoma, lymphoma, glioblastoma, head and neck cancer, and colon cancer, where it was 1 mm. Normal control blocks included kidney, tonsil, liver and colon. TMAs were constructed with the TMArrayer^{TM} (Pathology Devices, Inc.).

Immunohistochemistry

Antibodies were obtained from Cell Signaling Technology (CST) or from other sources as indicated: MET-pTyr1234/pTyr1235 (clone D26), MET4 [18], c-Met (clone SP44, Spring Bioscience), c-Met (clone D1C2), HGF (LifeSpan, BioSciences), Src-family-pTyr416, pErk1/2 (clone 137F5). Where needed, the specificity of antibodies was confirmed by western blotting before and after treatment with inhibitors (Figures S1A, S1B) [20]. The pSRC family-Tyr416 has not been optimized for IHC by the company (CST) and we therefore followed a published protocol [21], which we also validated in a neoadjuvant bladder cancer study [22]. The HGF antibody has been characterized in the Vande Woude laboratory [23] and our protocol provides a staining pattern that

is consistent with staining in mesenchymal cells. The specificity of the MET4 antibody was published in [18]. For each antibody, dilution, signal amplification and incubation conditions are listed in Table S2. Staining was performed as described previously [24]. Secondary antibodies were purchased from CST. The tyramide signal amplification system (TSA) was purchased from Perkin Elmer and the polymer amplification system was obtained from VECTOR labs. The immunofluorescent staining was performed with the Opal multiplex immunofluorescent system (Perkin Elmer) and fluorescent staining with $MET4^{EC}$ and $SP44\_MET^{IC}$ was followed by IHC with the pMET antibody.

For every core, the percent coefficient of variation (%CV) for between-days (five slides) or within-day (three slides) assays was calculated by dividing the mean core intensity by the standard deviation. The total %CV was calculated by first averaging the squares of individual %CV values followed by taking the square root this value.

The IHC staining variability amongst cores within a case was compared to the variability across cases using F-statistics. Details of calculations are provided in the material.

Digital image acquisition, image processing and pathology annotation of TMA cores

TMA slides were digitized on the high-resolution Leica SCN400NF whole-slide scanner and images were sequentially analyzed with the Tissue IA Optmiser (Leica) software installed on the Leica Digital Image Hub as described in [25]. Cancer and stromal areas were annotated by one of three pathologists and confirmed by second pathologist. The mean signal intensity (staining concentration) per unit area was calculated within annotated regions and exported for statistical analysis (Dataset S2).

Data acquisition and normalization

All statistical analyses were conducted in `R v3.1.3` [26]. Plots were generated with the use of the following packages in `R`, `beeswarm` [27], `extrafont` [28], `plyr` [29], `RColorBrewer` [30], `reshape2` [31], `scales` [32]. TMA data were subjected to background intensity subtraction (lowest core intensity of individual slide) and $\log_2$ transformation. Intensity values were normalized to the average signal intensities of kidney and tonsil control cores within respective slides. The final data represent the $\log_2$ transformed fold change from control. As a second normalization method, control adjusted TMA data values (without background subtraction) were quantile normalized across slides and antibodies using `limma` [33] package in `R`.

Determination of distributions and correlation coefficients

Histogram density profiles of each antibody were constructed using `ggplot2` [34] package in `R`. Unsupervised hierarchical clustering of pairwise Pearson's correlation matrix was calculated using `hclust` function based on Euclidean distance and complete linkage method. *p*-values of correlations generated for each antibody pair using data from all cancer types combined were adjusted using the stringent Bonferroni correction. *p*-values of pairwise correlations performed in cancer types individually were adjusted using the less stringent FDR correction [35]. Heatmaps were generated using `heatmap.2()` in `gplots` package [36]. The Dendrogram in Figure S5A of the correlation matrix was generated using `cluster` package [37]. The Wilcoxon rank-sum test was used to determine the significance of the difference between of T_HGF and St_HGF signal intensities.

pMET *z*-score

In order to compare average levels of pMET expressions across cancer types, *z*-scores of pMET staining intensities were calculated as the difference of the cancer-type mean and grand mean, divided by the standard deviation of all samples, and then multiplied by the square root of number of cases in that particular cancer type. See supplementary material for details of the calculations.

Random forest classification

The expression of pMET was dichotomized at the 7th decile to classify cases as positive or negative. Levels of pMET were predicted by fitting a Random Forest model to all data with the following features: cancer-type plus all antibodies, or cancer-type plus either 1 of the antibodies (MET4, SP44_MET, D1C2_MET, T_HGF, St_HGF). Random forest classification analyses were conducted using the `randomForest` function [38]. 10-fold cross validation was performed and the area under the curve (AUC) of the receiver operating characteristic (ROC) curves was determined for each model using the `ROCR` package [39]. Variable importance for each model was calculated using the `cforest` function in the `party` package [40–42].

Groups of five cancer-types ($n = 100$ cases) were constructed for all possible cancer-type combinations

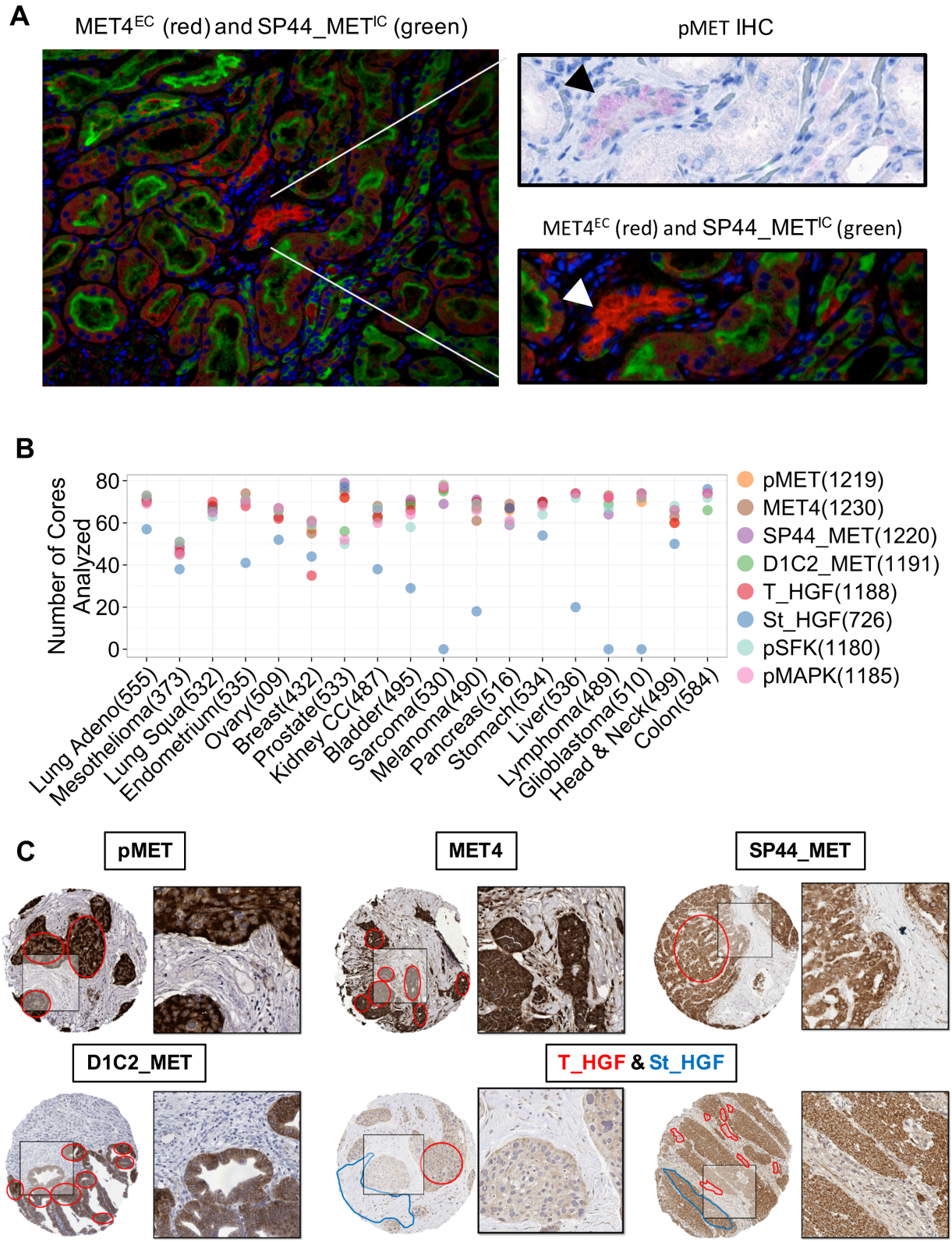

Figure 1.

($n = 8568$). Random Forest models were constructed in each group to predict pMET positivity with individual antibodies as predicting variables. Five-fold cross validation was performed for each model and the AUC was calculated.

Results

Differences in tissue staining between antibodies to the extra- and intracellular domain of MET

To identify potential differences in staining patterns of antibodies that react with the intracellular and extracellular domains of MET and with MET-pY1234/pY1235 (pMET), we stained tissue sections of renal cortex with α-pMET, SP44_MET^{IC} (antibody against MET intracellular domain) and MET4^{EC} (antibody against MET extracellular domain) (Figure 1A). Surprisingly, we observed marked heterogeneity of staining in renal tubules. In particular, individual cells in collecting duct epithelium preferentially reacted either with MET4^{EC} or SP44_MET^{IC}. Tubules that stained with α-pMET reacted with MET4^{EC,} but not with SP44_MET^{IC}. These data highlight cell specific differences in availability of the MET4^{EC} and SP44_MET^{IC} epitopes and suggest that antibodies against total MET protein might differ in their correlations with pMET levels. To take advantage of this result for development of companion diagnostics, we assembled a biomarker panel to investigate the relationship between MET phosphorylation, total MET protein expression, expression of HGF and activation of MET signalling pathways through SFK and MAPK.

Quantitative imaging of IHC with 7 antibodies in 18 cancer types

In order to test the MET-associated biomarker panel, we constructed a multi-cancer TMA consisting of 18 cancer types (lung adeno- and squamous carcinoma, mesothelioma, endometrium, ovary, breast, prostate, kidney clear cell, bladder, sarcoma, melanoma, pancreas, stomach, liver, lymphoma, glioblastoma, head and neck, and colon), 20 cases per cancer type and four cores per case (Figure S3, Dataset S1). In total, 1440 cores from 360 cases were displayed on seven glass slides. The average core loss after IHC was equally distributed across cancer types, such that 16–20 cases per cancer type provided data for statistical analysis. In addition, normal tissue cores were used for normalization and comparison of staining intensities across the seven slides.

Each TMA was stained with seven antibodies (Figures 1B, S3, Table S1). In order to overcome the problem of low sensitivity of measuring MET autophosphorylation at Y1234/Y1235 [43], we combined polymer and tyramide amplification systems without compromising the dynamic range (Figures S1C, S2B). The improved amplification method applied to α-pMET IHC resulted in TMA cores above the limit of quantification in all 18 cancer types. Control rabbit and mouse antibodies were negative (data not shown). We acquired 1180–1230 measurements per antibody in areas of cancer and 726 measurements in the stroma (Figure 1B). For all antibodies and cancer types together, we obtained 9139 measurements (Dataset S2).

To compare the staining intensities from each antibody across seven slides, we subtracted the background staining and calculated the fold change relative to control cores in the same slide (Figure S4). The resulting distributions of control-adjusted, $\log_2$-transformed staining intensities were normally distributed, ie, 'bell-shaped' (S2A). The expression of pMET levels in 18 cancer types is shown in Figure 2A. Phospho-MET staining was highest in bladder cancer and lymphoma. In addition, outlier cases with high pMET levels were identified in lung adenocarcinoma, endometrial, prostate, stomach and liver cancer, and in melanoma. In order to assess the biological variability, we compared expression values between cases to those within a case. Between-case variability was significantly higher than within-case variability (F-test, adjusted $p < 0.05$) (Figure 2B, Dataset S2), indicating that the within-tumour

Figure 1. Antibody-based analysis of the MET pathway in 18 cancer types. (A) SP44_MET^{IC} and MET4^{EC} staining in renal tubules. Normal kidney tissue was stained with SP44_MET^{IC} (green) and MET4^{EC} (red) by immunofluorescence and with α-pMET by immunohistochemistry (purple) and a representative case is shown. The low power image reveals heterogeneous staining patterns of the MET antibodies in multiple renal tubules. The arrow in the magnified panels points to the overlap between MET4^{IC} and α-pMET staining. (B) Data acquisition. 18 cancer types are listed and the numbers of cores with data are indicated in parentheses next to each cancer-type. Each cancer type was stained with seven antibodies. The total number of TMA cores providing data for each antibody is indicated in the legend. Number of cores analyzed per antibody in individual cancer types is plotted on the y-axis. (C) Specificity of antibody staining and annotation of cancer and stromal regions. Tissue cores were stained with antibodies indicated above each image and consist of areas of cancer and non-cancer tissue. The insert for each core shows an enlarged area of the cancer-to-stroma interface. For measurement of staining intensities, multiple areas in the cancer are circled in each core (red outline) and for cores stained with the HGF antibody, additional areas of stroma (blue) are circled for analysis.

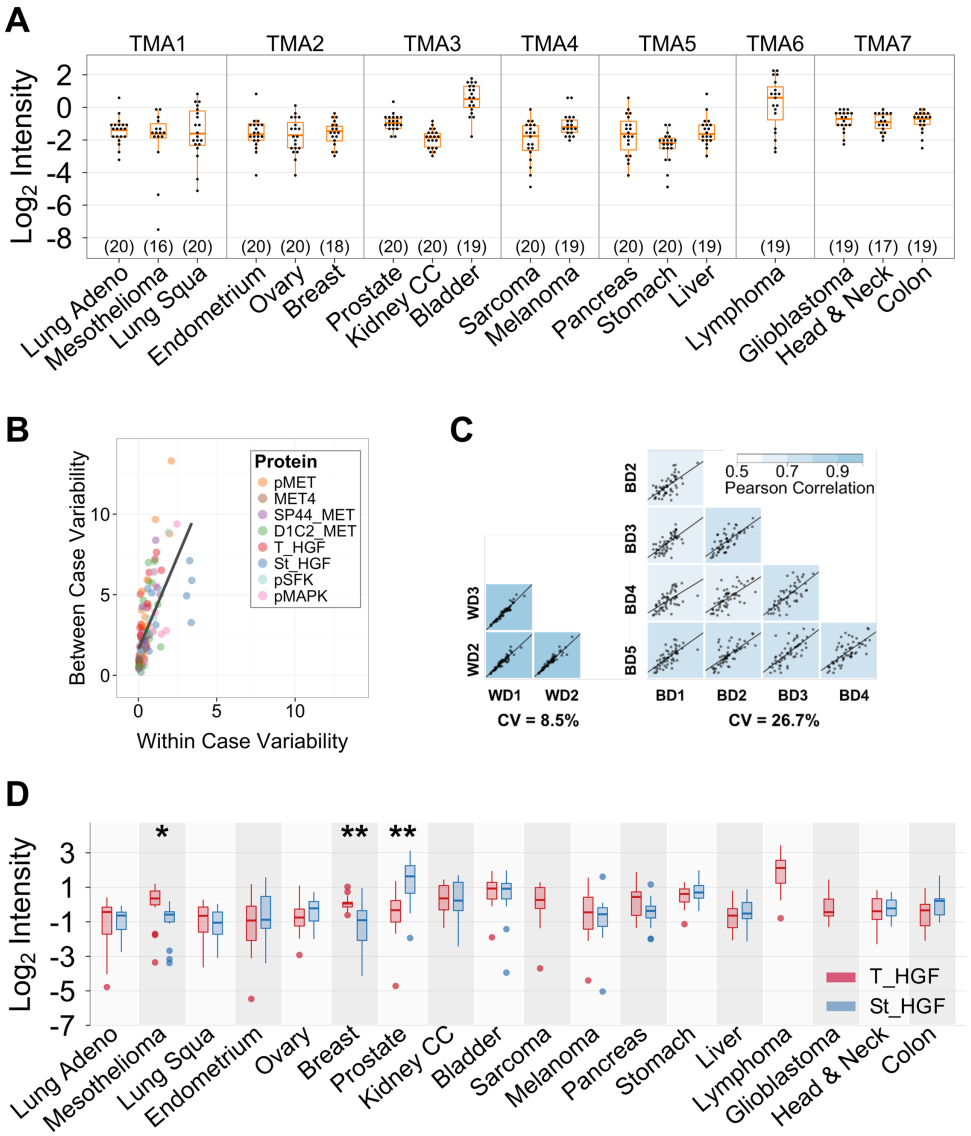

Figure 2. Protein expression levels. (A) Quantative imaging of pMET levels. Each TMA with its cancer types is listed on the x-axis and the number of cases per cancer type is listed in parentheses. Control-adjusted staining intensities are plotted on the y-axis. Horizontal lines in boxes represent the 1st, 2nd and 3rd quartiles. Whiskers are indicated outside the box with limits of 1.5× the interquartile range (IQR). (B) Inter- and intra-tumour variance. One-way analysis of variance was used to calculate the variance within cores of a case (within-case variability) and across all cases within a cancer type (between-case variability). Each colour indicates one of 18 cancer-types stained with a single antibody. (C) Within- and between-assay concordances. To determine within day (WD) technical variability of the assay, three slides of TMA 7 (WD1–3) were stained with the pMET antibody on the same day. To determine day-to-day variability, a single TMA 7 slide was stained on five different days (BD 1–5). Pairwise correlations for WD and BD slides are shown and the coefficients of variation (CV) are indicated for within day and between day variability. (D) HGF expression. The boxplots depict the control adjusted $\log_2$ expression of St_HGF and T_HGF in each cancer type. St_HGF expression could not be measured in cancer types that did not display sufficient regions of stroma with peritumoural mesenchymal cells (lymphoma, glioblastoma, sarcoma). A significant difference in expression between T_HGF and St_HGF is indicated by $^{**}p < 0.01$, $^{*}p < 0.05$.

heterogeneity was less than the heterogeneity exhibited across cases. Furthermore, the α-pMET within-day coefficient of variation (%CV) = 8.5% and the between-day %CV = 26.7%, both acceptable for IHC assays (Figure 2C) [44].

A switch from paracrine to autocrine HGF has been demonstrated during progression of AML and in the clonal selection of lung adenocarcinoma [8,45]. However, the prevalence of autocrine HGF in other primary solid tumours is not known. To determine the relationship

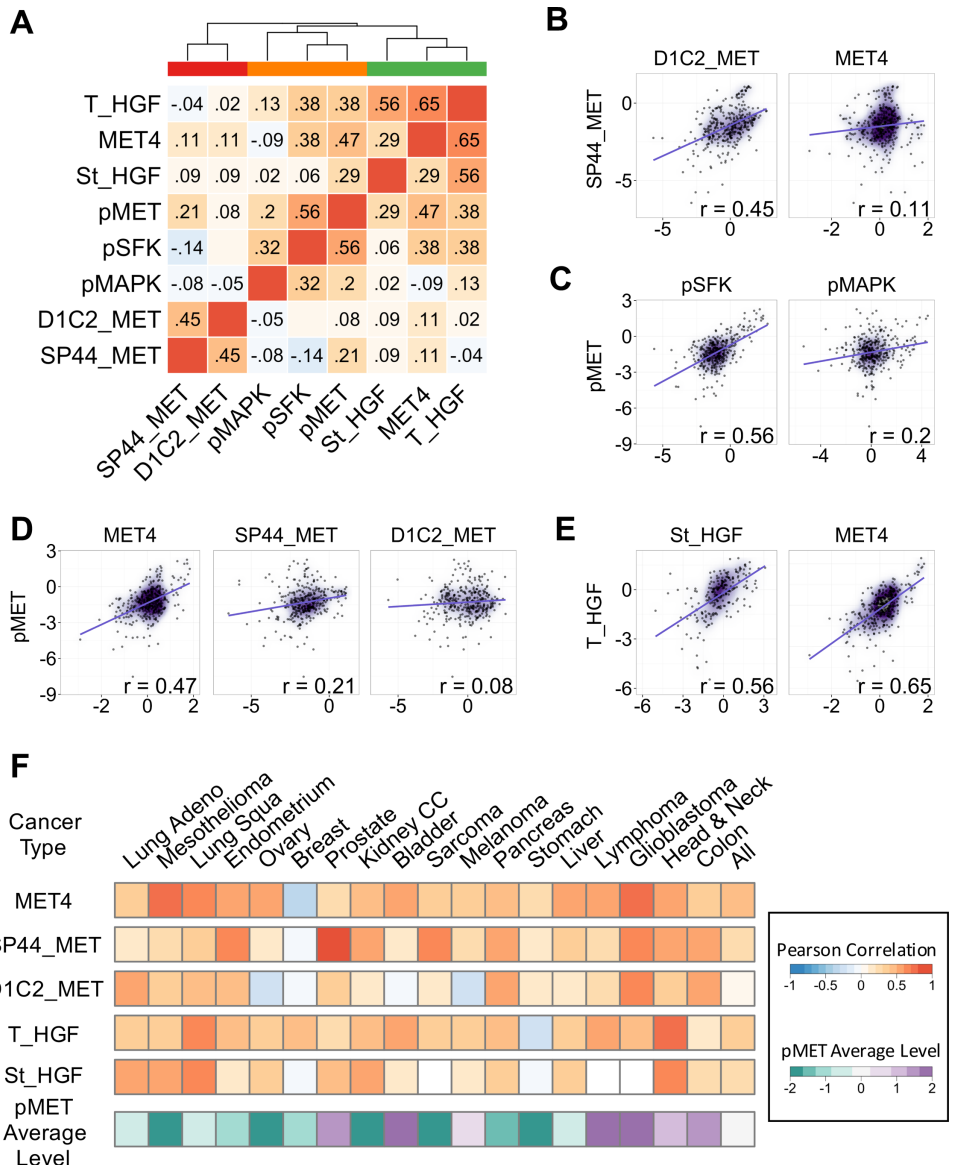

Figure 3. Correlations of protein expression levels determined by quantitative imaging (QI). (A) Correlation matrix for all cancer types. Pairwise correlations were calculated across all cases from 18 cancer types stained with the antibodies listed on the x- and y-axes. Pairwise correlation matrix was used in an unsupervised cluster analysis. The three main clusters are labelled above the matrix. (B–E) Scatter plots of normalized, relative staining intensities. A regression line is shown for each scatter plot and Pearson's correlation coefficients are indicated on the bottom right. (F) Correlations with pMET in individual cancer types. Pearson's correlation coefficients between levels of pMET and the MET and HGF antibodies listed next to the heatmap. The last row shows the pMET *z*-score (normalized average level), which was calculated by normalizing the average pMET level of an individual cancer type to the mean of pMET levels across all cancer types. Values in the heatmap are matched to the color bar.

between HGF expression and MET activation, we profiled tumour HGF levels (T_HGF) in 1188 cores from 18 different cancer types. In addition, we measured HGF levels in the stroma adjacent to tumour (St_HGF) in 726 cores. The highest stromal HGF levels were detected in prostate and stomach cancer (Figure 2D). In addition, tumour and stromal HGF were correlated ($r = 0.56$, $p < 0.001$) (Figure 3A).

Correlations between antibodies in the MET pathway and MET kinase activation

We reasoned that a better understanding of associations between antibodies that report the activation state of the MET pathway might allow for selection of surrogate biomarkers of MET activation. Thus, a correlation matrix was generated through

unsupervised clustering of pairwise correlations between the seven antibodies. The clustering revealed three major groups (Figures 3A, S5A). The first group consists of the SP44_MET^{IC} and D1C2_MET^{IC}, which both bind the C-terminus of the MET receptor. While measurements with SP44_MET^{IC} and D1C2_MET^{IC} were significantly correlated ($r = 0.45$, $p < 0.001$), correlations of the SP44_MET^{IC} and D1C2_MET^{IC} antibodies with MET4^{EC} were lower ($r = 0.11$, $p = 1$ and $r = 0.11$, $p = 1$, respectively) (Figures 3A, 3B, S5B). The second group contains all the phospho-antibodies. The highest correlation in this group is observed between α-pSFK and α-pMET ($r = 0.56$, $p < 0.001$). In contrast, the correlation between α-pMAPK and α-pMET is only $r = 0.20$ ($p = 0.0053$), suggesting greater pMET to pSFK than pMET to pMAPK signalling (Figure 3A, C). MET4^{EC} demonstrated the highest correlation with α-pMET ($r = 0.47$, $p < 0.001$), while correlation coefficients of SP44_MET^{IC} and D1C2_MET^{IC} with α-pMET were lower ($r = 0.21$ and $r = 0.08$, respectively) (Figure 3A, D). The third group consists of MET4^{EC}, T_HGF and St_HGF. T_HGF and St_HGF are significantly correlated ($r = 0.56$, $p < 0.001$) and, in addition, T_HGF is significantly correlated with MET4^{EC} (Figure 3E, $r = 0.65$, $p < 0.001$). Next, we performed an unsupervised hierarchical clustering analysis of pairwise correlation coefficients from 28 antibody pairs across the 18 cancer types (S6). Two major clusters were observed. The smaller cluster of five antibody pairs corresponds to pairs with the highest correlations in the correlation matrix in Figure 3A. To exclude a bias from the normalization method, we performed control-adjusted and quantile normalization method (S7) and observed similar correlation matrices (S8 and Figure 3A). In summary, the main observation from the correlation matrix is the stronger correlation between MET4^{EC} and α-pMET compared to either SP44_MET^{IC} or D1C2_MET^{IC} and α-pMET. In addition, MET4^{EC} is strongly correlated ($p < 0.001$) with T_HGF and α-pSFK.

MET protein expression and MET phosphorylation in individual cancer types

Since MET can be activated through overexpression, we determined the relationship between MET protein expression and MET receptor phosphorylation in individual cancer types. MET protein expression levels measured with MET4^{EC}, SP44_MET^{IC} and D1C2_MET^{IC} differed between cancer types (Figure S4A, one-way ANOVA, $p_{MET4} < 0.001$, $p_{SP44} < 0.001$, $p_{D1C2} < 0.001$). We calculated the correlation coefficients between pMET levels and total MET protein expression measured with MET4^{EC}, SP44_MET^{IC} or D1C2_MET^{IC} in individual cancer types (Figure 3F). Correlation coefficients $r > 0.5$ are twice as frequent for SP44_MET^{IC}/pMET than for D1C2_MET^{IC}/pMET (Figure S9A). Two cancer types (glioblastoma and endometrial) revealed high correlation coefficients ($r > 0.4$, FDR adjusted $p < 0.1$) for all three α-MET antibodies with α-pMET. The correlations with α-pMET in individual cancer types were not related to the z-score (normalized average level) of pMET expression ($p > 0.1$) (Figure S10). Collectively, the results demonstrate that across cancer types, MET4^{EC}, which reacts with an epitope in the extracellular domain, reports pMET more faithfully than the antibodies that bind the cytoplasmic C-terminus of MET and that MET activation and protein levels are not related.

Next, we determined the correlations between HGF and pMET expression in individual cancer types. Correlations $r \geq 0.5$ (FDR adjusted $p < 0.1$) between pMET and T_HGF were identified in four cancer types (head and neck, lymphoma, lung squamous and bladder carcinoma). While T_HGF ($r = 0.38$) and St_HGF ($r = 0.29$) were significantly correlated with pMET levels overall (Figures 3A, S5B), no correlation was observed with the z-scores of pMET levels ($p > 0.1$) (Figure S10). The results suggest that in some cancer types, either autocrine or paracrine HGF expression may contribute to the activation state of MET.

Predictive models of MET activation

The ultimate goal of this multi-cancer investigation is to compare the accuracy of antibodies for predicting MET activation. We applied a random forest (RF) classification approach to determine which antibodies singly or in combination best predict MET receptor phosphorylation. The activation state of the MET receptor was set at the 70th percentile cutoff of signal intensities of α-pMET. We constructed ROC curves using 10-fold cross validation for RF models that consisted either of a combination of all α-MET and α-HGF antibodies or of single antibodies. The accuracy of predicting pMET levels was based on the area under curve (AUC) (Figure 4A). In addition, a variable importance measurement is provided by the RF model for the contribution of each antibody and of the cancer type to the prediction. As previously noted, data normalized by both background with control adjustment or by quantile normalization methods generated similar results (Figure S11). The results from the RF prediction model underscore the important role of the cancer type in the prediction of MET activation status.

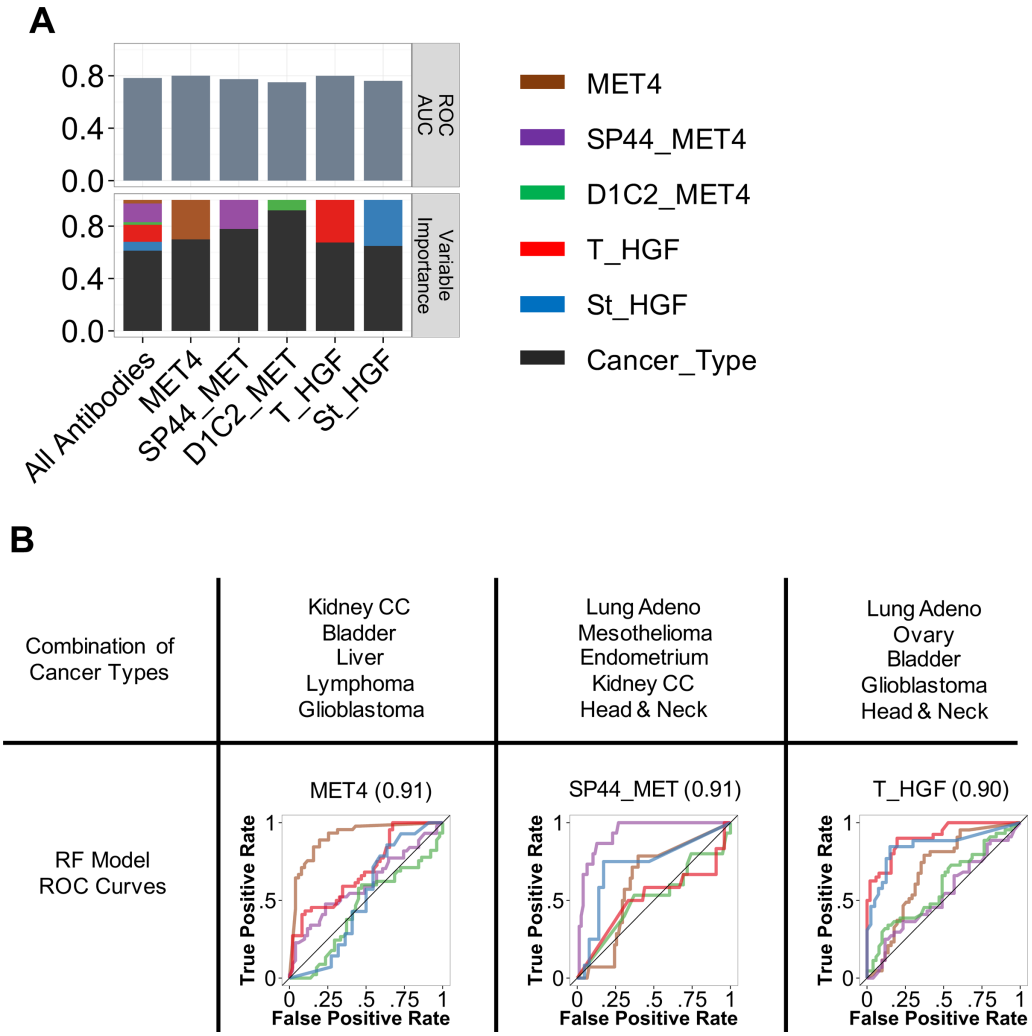

Figure 4. Random Forest (RF) models predicting MET activation status. (A) Variable importance. The y-axis of the top panel shows the AUC as determined by a RF model with 10-fold cross validation. Each bar depicts the total AUC from a model fitted with cancer type and antibodies indicated on the x-axis. The bottom panel shows the contributions of cancer type and antibody (RF variable importance) to the prediction by the model. The RF variable importance is shown on a scale from 0 to 1. (B) Prediction of pMET status in groups of five cancer types. Cases were combined from groups of five cancer types listed at the top. ROC curves were generated to determine the accuracy of the model predicting pMET activity status for each antibody (MET4^{EC}, SP44_MET^{IC} or T_HGF) with fivefold cross-validation. The AUC with the highest value across all possible combinations of five cancer types is shown for MET4^{EC}, SP44_MET^{IC} or T_HGF. ROC curves of St_HGF and D1C2_MET^{IC} are included for comparison.

To further examine the role of the cancer type in the prediction model, we combined data from five cancer types to increase the sample size. We also excluded D1C2_MET^{IC} and St_HGF from further evaluation because of the low variable importance of D1C2_MET^{IC} and the absence of St_HGF in some cancer types. Figure 4B shows the combinations of five cancer types with the greatest AUC for MET4^{EC}, SP44_MET^{IC} and T_HGF. These cancer type combinations were obtained from a total of 25,704 ROC curves for the three antibodies in all possible 5-cancer type combinations. Since a different combination of cancer types is obtained for each of the antibodies, the ROC curves confirm the important role of the cancer type in the prediction of pMET activation by MET4^{EC}, SP44_MET^{IC} and T_HGF.

Discussion

This study demonstrates for the first time that digital image analysis of IHC stained slides can be used as a general approach to improve the selection of

biomarkers for companion diagnostics to drugs targeting HGF/MET. We demonstrate that quantitative digital imaging (QI) can overcome difficulties of accurately measuring the inherently unstable and low abundance phosphorylation of the active MET receptor kinase in patient tissues by IHC. Replacing traditional categorical measurements with numerical measurements on a continuous scale improves the statistical data analysis in IHC assays. While a system for automated quantification of fluorescent antibody signals (AQUA) has been available for a long time [46], the method is not transferrable to chromogenic detection of antibody staining. In particular for IHC, QI lowers the limit of detection, reduces observer bias, lowers the technical variability and permits the normalization of experimental data to internal controls.

Using a robust pipeline we demonstrate that (1) it is feasible to measure levels of MET receptor activation and signalling in archival tissues from 18 cancer types; (2) in agreement with pre-clinical systems (reviewed in [3]), the magnitude of MET activation correlates with HGF and total MET protein expression levels; (3) an antibody reactive with an extracellular epitope in MET ($MET4^{EC}$) [18] more faithfully reports MET phosphorylation than antibodies that react with intracellular epitopes ($SP44\_MET^{IC}$, $D1C2\_MET^{IC}$); (4) intratumoural HGF expression levels predict MET activation more accurately than HGF expression in the tumour microenvironment [8,45], and (5) the prediction of MET activation is cancer type-specific. Collectively, the data provide novel insights into the choice of antibodies to measure the active MET receptor kinase and are consistent with cancer-type specific mechanisms of MET activation.

The comparison of MET antibodies that react with epitopes in the intracellular and extracellular domain of the receptor was prompted by the surprising differences of staining patterns in renal tubules (Figure 1A). The nature of MET receptor proteins that preferentially react with $MET4^{EC}$ versus $SP44\_MET^{IC}$ or $D1C2\_MET^{IC}$ is not known. $MET4^{EC}$ binds to an epitope in the 25 kDa alpha-chain of MET [18] and not to the transmembrane 140 kDa MET receptor beta-chain that interacts with $SP44\text{-}MET^{IC}$ and $D1C2\_MET^{IC}$ at its C-terminus. The MET C-terminal domain contains docking sites for multiple proteins that form a large signalling complex in response to MET kinase activation and autophosphorylation [47]. It is conceivable that this protein complex hinders the binding of $SP44\_MET^{IC}$ and $D1C2\_MET^{IC}$ to active MET, particularly after tissues are fixed by formalin treatment. The steric hindrance is also consistent with the weaker correlation of $SP44\_MET^{IC}$ and $D1C2\_MET^{IC}$ with α-pMET. In addition, $MET4^{EC}$ and α-pMET staining intensities correlate strongly with intratumoural HGF and with α-pSFK, suggesting that the heightened MET activation is associated with an HGF–MET–pSFK signalling axis (Figures 3A, S12). Previous measurements of tissue and plasma HGF in clinical trials with AMG-102 utilized HGF-specific ELISA assays and did not distinguish between intra- and extracellular HGF [48]. As confirmed by our prediction model, intratumoural HGF qualifies as a novel biomarker of MET activation status that might improve the prediction of pMET activation status.

There are limitations of this study that remain to be addressed. One is the true clinical predictive power of biomarkers in the MET pathway. While we have improved the reproducibility and sensitivity of detection of pMET through a combination of signal amplification and QI, the clinical significance of measuring pMET using this approach remains to be determined. It is also unclear whether pMET is sufficient as a treatment response biomarker and whether α-MET protein and α-HGF measurements are required to improve the prediction. Since phosphorylation is unstable and rapid fixation of biopsies is required to preserve the phosphoproteome [49], it is a reasonable assumption that antibodies that are not dependent on phosphorylation will be needed to determine the MET activation status in clinical samples. An answer to these questions can be obtained in the future by analysis of tissues from clinical trials with MET inhibitors. Another limitation is the small sample size of individual cancer types. Based on the marked differences of biomarker expression among cancer types, expanding cohorts of individual cancer types will be necessary to obtain conclusive results for each of the cancer types included in the study. Our attempts to build a prediction model by using 5-cancer type combinations is the most detailed analysis that our sample size permitted and the prediction of MET activation by MET4 and T_HGF expression levels is consistent with the correlations between pMET and MET4 or T-HGF.

The results in our study explain conclusions by others demonstrating the lack of strong correlation between MET expression and response to MET inhibitory antibodies [50–53] and highlight the importance of a cancer type specific development of companion diagnostics to MET inhibitory drugs.

Acknowledgements

We would like to thank Dr. Gary Gallick for the protocol used for the pSRC IHC. We would like to acknowledge the support from the Prostate Cancer Foundation, the Steven Spielberg Team Science Award, R01CA131255, R21CA118592, R21CA143618-02 (to

A.G.). We also acknowledge the institutional support and funding through the NIH G20 RR030860 to the Cedars-Sinai Biobank and Translational Research Core. The statistical data analysis by W.G.A. for this project has been funded in part with federal funds from the National Cancer Institute, National Institutes of Health, under contract No. HHSN261200800016C. The content of this publication does not necessarily reflect the views or policies of the Department of Health and Human Services, nor does any mention of trade names, commercial products, or organizations imply any endorsement by the U.S. Government.

Author Contributions

F.H., M.B.A., B.S.K designed study; Z.M., S.P., S.S., A.G., J.M., S.B., M.R., S.M.F. generated data; F.H., W.G.A., B.B. analyzed data; F.H., M.R.F., G.VW wrote the paper; X. Y., M.G., D.D., A.E.W., M. dP. V., A.M.M., D.J.L. created the Tissue Microarray.

References

1. Hamilton PW, Bankhead P, Wang Y, *et al*. Digital pathology and image analysis in tissue biomarker research. *Methods* 2014; **70:** 59–73.
2. Kumar A, Rao A, Bhavani S, *et al*. Automated analysis of immunohistochemistry images identifies candidate location biomarkers for cancers. *Proc Natl Acad Sci U S A* 2014; **111:** 18249–18254.
3. Gherardi E, Birchmeier W, Birchmeier C, *et al*. Targeting MET in cancer: rationale and progress. *Nat Rev Cancer* 2012; **12:** 89–103.
4. Jeffers M, Schmidt L, Nakaigawa N, *et al*. Activating mutations for the met tyrosine kinase receptor in human cancer. *Proc Natl Acad Sci U S A* 1997; **94:** 11445–11450.
5. Schmidt L, Duh FM, Chen F, *et al*. Germline and somatic mutations in the tyrosine kinase domain of the MET proto-oncogene in papillary renal carcinomas. *Nat Genet* 1997; **16:** 68–73.
6. Looyenga BD, Furge KA, Dykema KJ, *et al*. Chromosomal amplification of leucine-rich repeat kinase-2 (LRRK2) is required for oncogenic MET signaling in papillary renal and thyroid carcinomas. *Proc Natl Acad Sci U S A* 2011; **108:** 1439–1444.
7. Graveel C, Su Y, Koeman J, *et al*. Activating Met mutations produce unique tumor profiles in mice with selective duplication of the mutant allele. *Proc Natl Acad Sci U S A* 2004; **101:** 17198–17203.
8. Turke AB, Zejnullahu K, Wu YL, *et al*. Preexistence and clonal selection of MET amplification in EGFR mutant NSCLC. *Cancer Cell* 2010; **17:** 77–88.
9. Knudsen BS, Vande Woude G. Showering c-MET-dependent cancers with drugs. *Curr Opin Genet Dev* 2008; **18:** 87–96.
10. Varkaris A, Corn PG, Parikh NU, *et al*. Integrating murine and clinical trials with cabozantinib to understand roles of MET and VEGFR-2 as targets for growth inhibition of prostate cancer. *Clin Cancer Res* 2015; **22:** 107–121.
11. Furlan A, Kherrouche Z, Montagne R, *et al*. Thirty years of research on met receptor to move a biomarker from bench to bedside. *Cancer Res* 2014; **74:** 6737–6744.
12. Parachoniak CA, Luo Y, Abella JV, *et al*. GGA3 functions as a switch to promote Met receptor recycling, essential for sustained ERK and cell migration. *Dev Cell* 2011; **20:** 751–763.
13. Menard L, Parker PJ, Kermorgant S. Receptor tyrosine kinase c-Met controls the cytoskeleton from different endosomes via different pathways. *Nat Commun* 2014; **5:** 3907.
14. Hanna JA, Bordeaux J, Rimm DL, *et al*. The function, proteolytic processing, and histopathology of Met in cancer. *Adv Cancer Res* 2009; **103:** 1–23.
15. Watermann I, Schmitt B, Stellmacher F, *et al*. Improved diagnostics targeting c-MET in non-small cell lung cancer: expression, amplification and activation? *Diagn Pathol* 2015; **10:** 130.
16. Finocchiaro G, Toschi L, Gianoncelli L, *et al*. Prognostic and predictive value of MET deregulation in non-small cell lung cancer. *Ann Trans Med* 2015; **3:** 83.
17. Hack SP, Bruey JM, Koeppen H. HGF/MET-directed therapeutics in gastroesophageal cancer: a review of clinical and biomarker development. *Oncotarget* 2014; **5:** 2866–2880.
18. Knudsen BS, Zhao P, Resau J, *et al*. A novel multipurpose monoclonal antibody for evaluating human c-Met expression in preclinical and clinical settings. *Appl Immunohistochem Mol Morph* 2009; **17:** 57–67.
19. Collisson EA, Campbell JD *et al*. Comprehensive molecular profiling of lung adenocarcinoma. *Nature* 2014; **511:** 543–550.
20. Buchanan SG, Hendle J, Lee PS, *et al*. SGX523 is an exquisitely selective, ATP-competitive inhibitor of the MET receptor tyrosine kinase with antitumor activity in vivo. *Mol Cancer Ther* 2009; **8:** 3181–3190.
21. Kopetz S, Morris VK, Parikh N, *et al*. Src activity is modulated by oxaliplatin and correlates with outcomes after hepatectomy for metastatic colorectal cancer. *BMC Cancer* 2014; **14:** 660.
22. Hahn NM, Knudsen BS, Daneshmand S, *et al*. Neoadjuvant dasatinib for muscle-invasive bladder cancer with tissue analysis of biologic activity. *Urol Oncol* 2016; **34:** 4 e11–17.
23. Gao CF, Xie Q, Zhang YW, *et al*. Therapeutic potential of hepatocyte growth factor/scatter factor neutralizing antibodies: inhibition of tumor growth in both autocrine and paracrine hepatocyte growth factor/scatter factor:c-Met-driven models of leiomyosarcoma. *Mol Cancer Ther* 2009; **8:** 2803–2810.
24. Akfirat C, Zhang X, Ventura A, *et al*. Tumour cell survival mechanisms in lethal metastatic prostate cancer differ between bone and soft tissue metastases. *J Pathol* 2013; **230:** 291–297.
25. Gertych A, Mohan S, Maclary S, *et al*. Effects of tissue decalcification on the quantification of breast cancer biomarkers by digital image analysis. *Diagn Pathol* 2014; **9:** 213.
26. R Development Core Team. R: A Language and Environment for Statistical Computing. Vienna, Austria: the R Foundation for Statistical Computing. 2015. Available at http://www.R-project.org/.
27. Eklund A. beeswarm: The Bee Swarm Plot, an Alternative to Stripchart, R package version 0.2.0. 2015. Available at https://CRAN.R-project.org/package=beeswarm.
28. Chang W. Extrafont: Tools for using fonts, R package version 0.17. 2014. Available at https://CRAN.R-project.org/package=extrafont.
29. Wickham H. The split-apply-combine strategy for data analysis. *J Stat Softw* 2011; **40:** 1–29.

30. Neuwirth E. RColorBrewer: ColorBrewer Palettes, R package version 1.1-2. 2014. Available at https://CRAN.R-project.org/package=RColorBrewer.
31. Wickham H. Reshaping data with the reshape package. *J Stat Softw* 2007; **21:** 1–20.
32. Wickham H. Scales: Scale Functions for Visualization, R package version 0.2.5. 2015. Available at https://CRAN.R-project.org/package=scales.
33. Ritchie ME, Phipson B, Wu D, *et al*. Limma powers differential expression analyses for RNA-sequencing and microarray studies. *Nucleic Acids Res* 2015; **43:** doi: 10.1093/nar/gkv1007.
34. Wickham H. ggplot2: Elegant Graphics for Data Analysis. Springer: New York, 2009.
35. Benjamini Y, Hochberg Y. Controlling the false discovery rate: a practical and powerful approach to multiple testing. *J R Stat Soc Series B Stat Methodol* 1995; **57:** 289–300.
36. Gregory R. Warnes BB, Lodewijk Bonebakker, Robert Gentleman, Wolfgang Huber, Andy Liaw, Thomas Lumley, Martin Maechler, Arni Magnusson, Steffen Moeller, Marc Schwartz and Bill Venables. gplots: Various R Programming Tools for Plotting Data, R package version 2.17.0. 2015. Available at https://CRAN.R-project.org/package=gplots.
37. Maechler M, Rousseeuw P, Struyf A, *et al*. Cluster: Cluster Analysis Basics and Extensions, R package version 2.0.1. 2015. Available at https://CRAN.R-project.org/package=cluster.
38. Liaw A, Wiener M. Classification and regression by randomForest. *R News* 2002; **2:** 18–22.
39. Sing T, Sander O, Beerenwinkel N, *et al*. ROCR: visualizing classifier performance in R. *Bioinformatics* 2005; **21:** 7881.
40. Hothorn T, Buhlmann P, Dudoit S, *et al*. Survival ensembles. *Biostatistics* 2006; **7:** 355–373.
41. Strobl C, Boulesteix AL, Kneib T, *et al*. Conditional variable importance for random forests. *BMC Bioinformatics* 2008; **9:** 307.
42. Strobl C, Boulesteix AL, Zeileis A, *et al*. Bias in random forest variable importance measures: illustrations, sources and a solution. *BMC Bioinformatics* 2007; **8:** 25.
43. Jarantow SW, Bushey B, Pardinas JR, *et al*. Impact of cell-surface antigen expression on target engagement and function of an EGFR x c-Met bispecific antibody. *J Biol Chem* 2015; **290:** 24689–24704.
44. Reed GF, Lynn F, Meade BD. Use of coefficient of variation in assessing variability of quantitative assays. *Clin Diagn Lab Immunol* 2002; **9:** 1235–1239.
45. Kentsis A, Reed C, Rice KL, *et al*. Autocrine activation of the MET receptor tyrosine kinase in acute myeloid leukemia. *Nat Med* 2012; **18:** 1118–1122.
46. Rubin MA, Zerkowski MP, Camp RL, *et al*. Quantitative determination of expression of the prostate cancer protein alpha-methylacyl-CoA racemase using automated quantitative analysis (AQUA): a novel paradigm for automated and continuous biomarker measurements. *Am J Pathol* 2004; **164:** 831–840.
47. Birchmeier C, Birchmeier W, Gherardi E, *et al*. Met, metastasis, motility and more. *Nat Rev Mol Cell Biol* 2003; **4:** 915–925.
48. Zhang Y, Doshi S, Zhu M. Pharmacokinetics and pharmacodynamics of rilotumumab: a decade of experience in preclinical and clinical cancer research. *Br J Clin Pharmacol* 2015; **80:** 957–964.
49. Bai Y, Cheng H, Bordeaux J, *et al*. Comparison of HER2 and phospho-HER2 expression between biopsy and resected breast cancer specimens using a quantitative assessment method. *PLoS One* 2013; **8:** e79901.
50. Lacroix L, Post SF, Valent A, *et al*. MET genetic abnormalities unreliable for patient selection for therapeutic intervention in oropharyngeal squamous cell carcinoma. *PLoS One* 2014; **9:** e84319.
51. Watermann I, Schmitt B, Stellmacher F, *et al*. Improved diagnostics targeting c-MET in non-small cell lung cancer: expression, amplification and activation? *Diagn Pathol* 2015; **10:** 130.
52. Koeppen H, Yu W, Zha J, *et al*. Biomarker analyses from a placebo-controlled phase II study evaluating erlotinib+/-onartuzumab in advanced non-small cell lung cancer: MET expression levels are predictive of patient benefit. *Clin Cancer Res* 2014; **20:** 4488–4498.
53. Jurmeister P, Lenze D, Berg E, *et al*. Parallel screening for ALK, MET and ROS1 alterations in non-small cell lung cancer with implications for daily routine testing. *Lung Cancer* 2015; **87:** 122–129.

SUPPLEMENTARY MATERIAL ONLINE

Supplementary materials and methods

Figure S1. Specificity of antibodies. (A) Specificity of MET antibodies. (B) Specificity of pSRC and pMAPK antibodies. (C) Scatterplot of pMET intensities

Figure S2. TMA data distribution and dynamic range. (A) Distribution of signal intensities for each antibody. (B) Dynamic ranges of antibody measurements

Figure S3. Workflow of case selection, tissue microarray (TMA), and digital image data acquisition

Figure S4. Boxplots of protein expression in 18 cancer types and kidney and tonsil controls. (A) Boxplots of anti-MET antibodies. (B) Boxplots of T_HGF, St_HGF, pMAPK, pSFK. (C) Examples of IHC for pMET, MET4 and SP44_MET

Figure S5. Dendrogram and p-values for correlation matrix Figure 3A. (A) Dendrogram of hierarchical clustering. (B) p-values of pairwise Pearson correlation coefficients

Figure S6. Unsupervised cluster analysis of pairwise Pearson correlation coefficients

Figure S7. Comparison of 2 normalization methods for protein expression measurements. (A) Comparison of two normalization methods across slides. (B) Boxplots of normalized expression measurements for individual antibodies

Figure S8. Analysis of quantile normalized data. (A) Correlation matrix. (B) Scatterplots of pMET, 3 MET antibodies and HGF expression in all cancer types for quantile normalized data

Figure S9. Scatterplots of pMET, MET and HGF expression levels. (A) Scatterplots of pMET and antibodies reactive with MET protein. (B) Scatter plot of pMET and HGF expression levels

Figure S10. Scatterplots of pMET *z*-scores and pMET correlation coefficients

Figure S11. Model performance and variable importance of quantile normalized data

Figure S12. Schematic diagram of MET receptor pathway and the binding sites of antibodies used in the study

Table S1. Tissue Microarray construction profiles

Table S2. Antibodies and staining conditions for immunohistochemistry

Dataset S1

Dataset S2